Supplement of Atmos. Chem. Phys., 26, 16873–16893, 2026
https://doi.org/10.5194/acp-26-16873-2026-supplement
© Author(s) 2026. CC BY 4.0 License.



Atmospheric Chemistry and Physics
Open Access
EGU

Supplement of

Technical note: A decoupled in situ framework for aerosol multi-wavelength optical properties: application for lidar retrievals

Cheng Yao et al.

Correspondence to: Longlong Wang (longlong.wang@zjnu.edu.cn)

The copyright of individual parts of the supplement might differ from the article licence.

S1 Measurement configuration, derived diagnostics, and cohort construction

S1.1 Measurement configuration

The SMPS, OPC, and AE33 measurements were acquired through separate sampling lines. The GRIMM SMPS+C with a long differential mobility analyser was operated at aerosol and sheath flows of 0.3 and 3.0 L min^{-1}. The GRIMM 1.109 OPC sampled through a TSP-type inlet at 1.2 L min^{-1}, whereas the AE33 used a separate $PM_{2.5}$ inlet at 5 L min^{-1}. The nominal sampling-line length was approximately 3 m with 6.35 mm tubing. These instrument streams were synchronized to the hourly analysis grid before the response-constrained PSD reconstruction.

Table S1. Measurement configuration and diagnostic roles.

Stream	Configuration	Use in the analysis	Interpretive boundary
GRIMM SMPS+C	L-DMA; 0.3 L min^{-1} aerosol flow; 3.0 L min^{-1} sheath flow	Fine-mode number-size distribution and $PM_{1,\,ref}$ loading criterion	Not an independent optical reference
GRIMM 1.109 OPC	TSP-type inlet; nominal flow 1.2 L min^{-1}	Coarse-mode size information after response-aware diameter remapping	Single-wavelength response model; coarse-tail transmission remains a structural uncertainty
AE33	Separate $PM_{2.5}$ inlet; 5 L min^{-1}	Multi-wavelength absorption constraint and AAE/eBC diagnostics	eBC and absorption share the same measurement and C_{eff} assumption
Station RH	Hourly collocated near-surface RH	Post-inversion hygroscopic-growth calculation	Near-surface ambient-equivalent calculation; not a vertically resolved lidar measurement

S1.2 Sampling-line transmission considerations

Because no direct transmission measurement was available for the Vipava configuration, size-dependent losses were not corrected. Published GRIMM 1.109 configurations with comparable tubing diameters and lengths indicate limited transmission losses below several micrometres, but these values are used only as contextual benchmarks and are not transferred quantitatively to the present campaign.

For context, Lill et al. (2024) used the same GRIMM 1.109 at the same flow rate with an approximately 1.5-m vertical 6.35 mm line and estimated transmission of approximately 99–88% over 0.25–10 µm. Zinke et al. (2024) similarly operated a GRIMM 1.109 through a 5-m vertically downward 6.35 mm line with a 180° bend and explicitly evaluated diffusion, impaction, and sedimentation losses, which contributed only approximately 0.6–1.5% across their analysed 0.25–2.5 µm size range. We use these results only as configuration-based benchmarks rather than transferring their transmission efficiencies directly to Vipava.

S1.3 Derived diagnostics

PSD-derived $PM_{2.5}$ and PM_{10} were calculated as diagnostic dry-state mass-equivalent quantities rather than independent mass measurements. The size-resolved number distribution was converted to mass using densities of 1.8 g cm^{-3} for $D_g \leq 1$ µm and 2.62 g cm^{-3} for $D_g > 1$ µm. Geometric-equivalent diameters were approximated as aerodynamic-equivalent diameters using a unit dynamic shape factor and a reference density of $\rho_0 = 1$ g cm^{-3}; the mass distribution was then integrated across the $PM_{2.5}$ and PM_{10} aerodynamic cut-offs with fractional treatment of intersecting bins.

The eBC time series was derived from AE33 absorption at 880 nm using the stated C_{eff} scenario and MAC_{880} = 7.77 m² g⁻¹. It is therefore an AE33-derived loading indicator rather than an independent constraint on C_{eff}.

S1.4 Cohort construction

The analysis-specific cohorts were then defined from the fixed hourly grid using the availability, precipitation, loading, numerical-validity, and post-retrieval screens summarized in Table S2. Their temporal disposition is shown in Fig. S1.

Table S2. Cohort accounting and analysis-specific subsets.

Stage	N	Definition	Application
Fixed hourly analysis grid	385	All hourly records within campaign period	Common temporal reference
Hard-valid candidates	309	Passed input availability, precipitation, loading and numerical-validity screens ($PM_{1,ref} \geq 3$ µg m⁻³; Di Antonio et al., 2025)	Overlap and retrieval diagnostics
Final post-QC cohort	304	Hard-valid candidates with $n_{655} \geq 1.33$	Main statistics and sensitivity analyses
$C_{eff}/C_{eff}(\lambda)$ paired cohort	303	Valid under both absorption correction schemes	C_{eff} spectral sensitivity
RH-active subset	275	Final cohort with RH-driven growth correction active	RH response analysis
Uncapped RH subset	260	Final-cohort hours with 40% ≤ RH ≤ 95%	RH cap sensitivity
Low-RH operational-reference subset	29	Final-cohort hours with RH < 40%, GF = 1	Low-RH reference
RH-capped subset	15	Hours with measured RH above 95%; RH input capped at 95% for the forward calculation	RH-cap treatment and sensitivity
Synthetic cases	480	Prescribed forward-inverse experiments	Numerical closure analysis

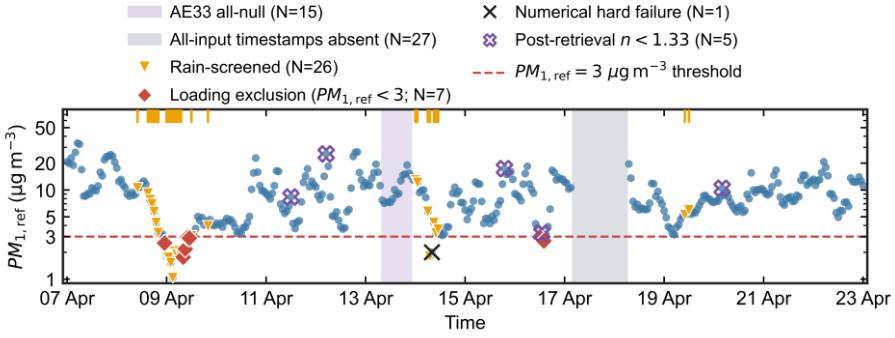


Figure S1. Campaign context and data availability on the fixed hourly analysis grid (N=385). Breaks indicate unavailable or screened hours and are retained as gaps rather than interpolated. Optical diagnostics are displayed only where the required inputs and retrieval outputs satisfy the stated analysis screens.

S2 SMPS–OPC overlap diagnostics and real-refractive-index identifiability

The pre-blend overlap was evaluated after the final best-fit n had been obtained, using two descriptive diagnostics computed between the measured SMPS distribution and the unscaled, response-remapped OPC distribution on the common 350–750 nm overlap grid. Let x_i and y_i denote $\log_{10}$ number concentrations, and let the overbar denote the mean over the N_{eff} valid common-support points. The demeaned shape RMSE is

$$Q_{shape} = \sqrt{\frac{\sum_i [(x_i - \bar{x}) - (y_i - \bar{y})]^2}{N_{\mathrm{eff}}}} \tag{S1}$$

The relative amplitude consistency is represented by

$$A_{SMPS/OPC} = 10^{median(x_i - y_i)} \tag{S2}$$

Thus, Q_{shape} quantifies the pre-blend overlap-region shape mismatch after removal of a common amplitude offset, whereas $A_{\mathrm{SMPS/OPC}}$ characterizes the relative concentration-scale offset between the measured SMPS and response-remapped OPC distributions. For the final N = 304 cohort, the median (IQR) values were 0.221 (0.172–0.276) for Q_{shape} and 0.978 (0.600–1.434) for $A_{\mathrm{SMPS/OPC}}$. Both were descriptive post-fit diagnostics: neither was included in $J(n)$, used to determine the best-fit n, nor used to trigger exclusion because no independently validated rejection threshold was available. The identifiability of the retrieved real refractive index was assessed from the objective-function profile $J(n)$, evaluated over the LUT range $1.30 \le n \le 1.70$.

For each candidate n, the log-space residual at overlap-grid point i was defined as

$$d_i(n) = \log_{10} N_{SMPS,i}^{obs} - \log_{10} \tilde{N}_i^{cand}(n) \tag{S3}$$

where $\tilde{N}_i^{cand}(n)$ is the trial-n candidate merged number concentration on the common grid, constructed by response-remapping the OPC distribution and then combining it with the SMPS distribution. The shape-consistency objective was then defined as

$$J(n) = \frac{1}{M(n)} \sum_{i=1}^{M(n)} \rho_{0.5}\left[d_i(n) - \bar{d}(n) \right], \quad \bar{d}(n) = \frac{1}{M(n)} \sum_{i=1}^{M(n)} d_i(n) \tag{S4}$$

where $M(n)$ is the number of retained grid points in the 350–750 nm overlap interval at which both distributions exceed 10^{-6} cm^{-3}, and $\rho_{0.5}$ denotes the Huber loss with transition parameter δ=0.5. Subtracting the mean residual removes a common log-space amplitude offset, so $J(n)$ quantifies mismatch in distribution shape rather than in absolute concentration.

Therefore, the profile describes how strongly the available optical and size-distribution constraints favour different real refractive-index solutions, rather than the smoothness of the merged PSD alone.

Within the fixed LUT range $1.30 \le n \le 1.70$, the descriptive relative-5% support comprises trial values satisfying $[J(n) - J_{\min}] / [J_{\max} - J_{\min}] \le 0.05$. The width $W_{5\%}$ is the span from the lowest to the highest selected n, including gaps between support components. It describes relative objective-profile support, not a statistically calibrated uncertainty interval. Of the final 304 profiles, 287 have support contained within the LUT, while 8 and 9 reach its lower and upper boundaries, respectively. The best-fit solutions for these 17 cases remain internal; support

beyond the evaluated LUT has not been assessed. The median $W_{5\%}$ is 0.078 (interquartile range: 0.054–0.102). Using 0.10, one-quarter of the LUT span, as a descriptive width reference, 84 profiles (27.6%) have $W_{5\%} \geq 0.10$; 16 also reach a boundary. This reference is used for reporting, not as a validated quality threshold or an additional screening criterion.

For the full cohort, the mean and median n_{655} are 1.4399 and 1.4155. Omitting boundary-contact cases only from the statistical summary gives 1.4377 and 1.4124 (N=287). The subset with $W_{5\%} < 0.10$ has a mean of 1.4205 and a median of 1.3886 (N=220). These comparisons describe differences between subsets, not retrieval bias or evidence of greater accuracy for narrower-support cases. No additional screening criterion is introduced: the final cohort remains the 304 retrievals obtained after excluding five of the 309 hard-valid candidates using the operational $n_{655} \geq 1.33$ plausibility screen.

The definitions, inferential roles, and QC treatment of these diagnostics are summarized in Table S3, while objective-profile support and structural sensitivity are shown in Fig. S2.

Table S3. Definitions, reporting conventions, and QA/QC treatment of overlap and identifiability diagnostics.

Quantity	Definition	Role	QC treatment
Q_{shape}	Demeaned $\log_{10}$-space SMPS–OPC shape RMSE at best-fit n	Pre-blend shape mismatch	Continuous diagnostic; no empirical rejection threshold
$A_{SMPS/OPC}$	10 to the median SMPS–OPC $\log_{10}$ amplitude offset	Relative concentration-scale consistency	Continuous diagnostic; A=1 denotes amplitude agreement
$J(n)$	De-meaned Huber shape objective for the SMPS–candidate merged PSD residual	Trial-n objective profile	Used to rank trial n values; not an independent PSD-validation metric
$W_{5\%}$	Width of the relative-5 % near-optimal support of $J(n)$	Descriptive identifiability indicator	Not a confidence interval and not used alone for exclusion
LUT contact	Near-optimal support intersects n = 1.30 or 1.70	Boundary-sensitivity flag	Retained if the best fit is internal and the profile is finite
$n_{655} \geq 1.33$	Operational lower-RRI plausibility criterion	Post-retrieval plausibility screen	Five hard-valid candidates excluded (Sinyuk et al., 2020)

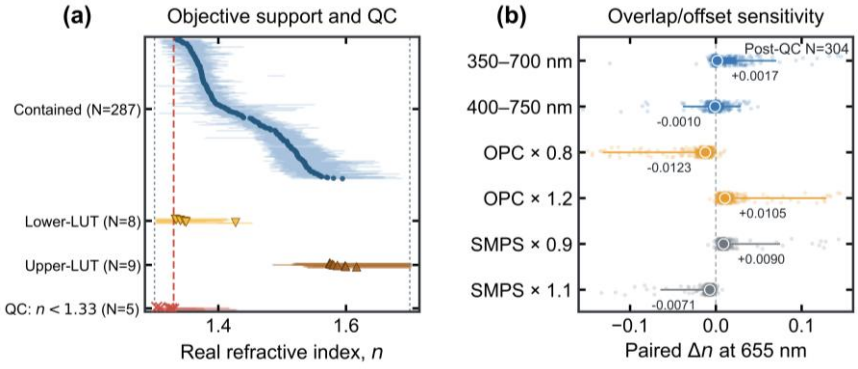


Figure S2. Objective-profile support and structural sensitivity of n_{655}. (a) Descriptive 5%-support intervals and best-fit values for 309 candidates; the dashed red line marks n_{655} = 1.33. Of 304 retained profiles, 287 supports were contained within the LUT, 8

were lower-LUT-sensitive, and 9 upper-LUT-sensitive. (b) Paired changes in n_{655} under alternative overlap intervals and SMPS/OPC offsets. Circles, thick bars, and thin bars denote medians, IQRs, and P2.5–P97.5, respectively.

S3 Monte Carlo propagation of measurement-input uncertainty

For each retained hourly retrieval, 500 realizations were requested. Measurement inputs were perturbed with mean-one lognormal factors. For a prescribed relative standard deviation r and a standard-normal deviate Z, the multiplicative factor was

$$F_i^{(k)} = \exp\left(\sigma_{\ln,i} Z_i^{(k)} - \frac{\sigma_{\ln,i}^2}{2}\right), \quad \sigma_{\ln,i} = \sqrt{\ln\left(1 + r_i^2\right)} \tag{S5}$$

SMPS size bins and OPC channels were sampled independently, AE33 absorption perturbations were sampled independently by wavelength, and the three instrument groups were mutually independent. MC summaries were calculated from realizations satisfying the predefined retrieval-validity criteria. This ensemble propagates the stated measurement-input perturbations only; it does not sample C_{eff} or $C_{\mathrm{eff}}(\lambda)$, overlap/remapping structure, hygroscopicity, particle shape, or homogeneous-equivalent mixing.

Table S4. Monte Carlo perturbation contract and separation from other uncertainty classes.

Source/class	Magnitude and distribution	Correlation structure	Reporting interpretation
SMPS number concentration	10% relative SD; multiplicative mean-one lognormal	Independent among size bins; independent of OPC and AE33	MC-propagated measurement-input spread
OPC number concentration	20% relative SD; multiplicative mean-one lognormal	Independent among OPC channels; independent of SMPS and AE33	MC-propagated measurement-input spread
AE33 absorption	20% relative SD; multiplicative mean-one lognormal	Independent among wavelengths; independent of SMPS and OPC	MC-propagated measurement-input spread
Campaign variability	Across-hour SD and percentiles for N = 304	Observed hourly variation	Source of campaign mean±SD; not MC uncertainty
Deterministic structural sensitivity	Alternative $C_{\mathrm{eff}}/C_{\mathrm{eff}}(\lambda)$, overlap windows, concentration offsets, PSD cut-offs, and RH treatments	Scenario-specific paired reruns	Reported as paired changes; not confidence intervals
Fixed/model-form limitations	κ values, spherical Mie optics, homogeneous-equivalent mixing	Not sampled in the MC ensemble	Qualitative or separately bounded limitation; no total uncertainty claim

S4 Sensitivity to AE33 multiple-scattering correction assumptions

The scalar C_{eff}=5 case is retained as a reference sensitivity scenario, not as an independently calibrated constant. A literature-informed wavelength-dependent profile was constructed from the UGR-average reference data (Yus-Díez et al., 2025), normalized to C_{355}=5, and used to repeat the complete retrieval chain. The tested profile gives C_{532}=4.36, C_{655}=4.12, and C_{1064}=4.61. Because no paired campaign absorption reference exists at 1064 nm, the profile is a structural sensitivity scenario and not a campaign-specific calibration.

Table S5 defines the two correction scenarios and their inferential roles, whereas Fig. S3 compares their effects on spectral *k*, lidar ratio, spectral ordering, and regime-level responses for the common N = 303 cohort.

Table S5. AE33 correction scenarios and inferential role.

Scenario	C_{355}	C_{532}	C_{655}	C_{1064}	Interpretation
Scalar reference	5.00	5.00	5.00	5.00	Reference sensitivity setting; not independently calibrated
Tested $C_{eff}(\lambda)$	5.00	4.36	4.12	4.61	UGR-average literature-informed structural sensitivity profile

The common paired cohort valid under both correction schemes contains N=303 hours. Median k retained the tendency toward larger values at shorter wavelengths, and the campaign-level LR ordering toward lower values at 1064 nm was preserved. The fraction of individual hours satisfying strict spectral ordering was more sensitive, which limits claims about detailed hour-by-hour absorption-related spectral behaviour. FVF-regime contrasts and paired LR_{1064} magnitudes were therefore evaluated explicitly rather than inferred from the median spectrum alone.

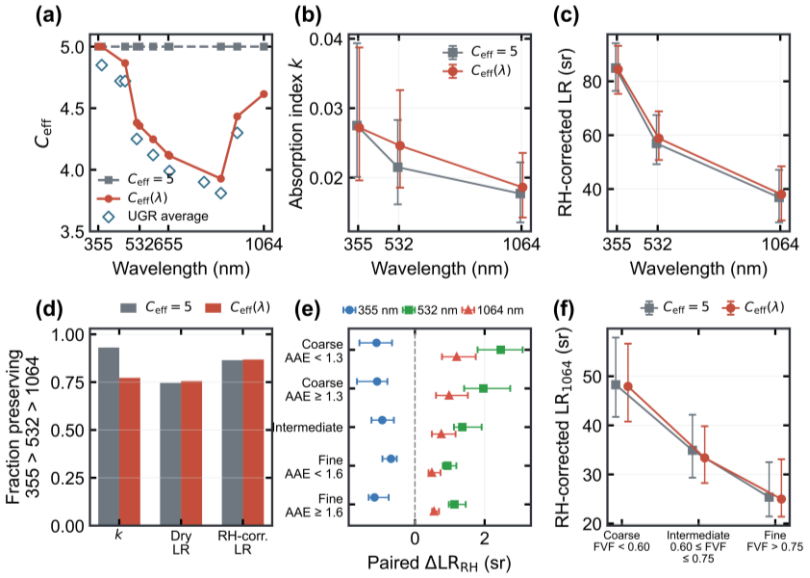


Figure S3. Sensitivity of retrieved lidar-relevant optical products to the wavelength-dependent C_{eff} (λ) scenario for the common N = 303 cohort. (a) Tested correction schemes; (b) spectral absorption index k; (c) RH-corrected lidar ratio; (d) fraction preserving strict 355 > 532 > 1064 ordering; (e) paired regime-level LR changes; and (f) paired LR_{1064}. Error bars and distribution summaries are defined in the panels. This is a structural sensitivity test, not a calibration of C_{eff}.

S5 Sensitivity to coarse-particle PSD support and particle-shape limitations

The dry reconstructed PSD was truncated at D_{max}=2.5, 5, and 10 μm and compared with the full PSD extending to approximately 20 μm. Refractive index, RH, hygroscopicity parameters, and wet-state mixing were held fixed, and concentrations below each cut-off were not renormalized. This design isolates the response to coarse-size support rather than re-optimizing the inversion.

The paired lidar-ratio changes are summarized in Table S6, while Fig. S4 shows the cumulative size-resolved extinction and backscatter contributions that explain the stronger 1064 nm sensitivity.

Table S6. Median RH-corrected lidar ratios and median paired hourly relative changes under PSD upper-diameter truncation.

D_{max}	Median LR_{1064} (sr)	ΔLR_{355}	ΔLR_{532}	ΔLR_{1064}
2.5 µm	33.88	−1.47%	−3.12%	−8.79%
5 µm	34.80	−0.95%	−2.10%	−7.95%
10 µm	36.69	−0.38%	−0.85%	−3.46%
≈20 µm (full PSD)	38.27	Reference	Reference	Reference

For the N = 304 post-QC cohort, the full-PSD median RH-corrected LR_{1064} was 38.27 sr. Truncation reduced, rather than increased, LR_{1064}, while the campaign-level ordering $LR_{355} > LR_{532} > LR_{1064}$ remained unchanged. At 1064 nm, particles below 2.5, 5, and 10 µm contributed 84.48%, 90.60%, and 96.10% of extinction, compared with 92.78%, 98.45%, and 99.69% of backscatter. The coarse tail therefore contributes proportionally more to extinction than to backscatter within the spherical-Mie calculation.

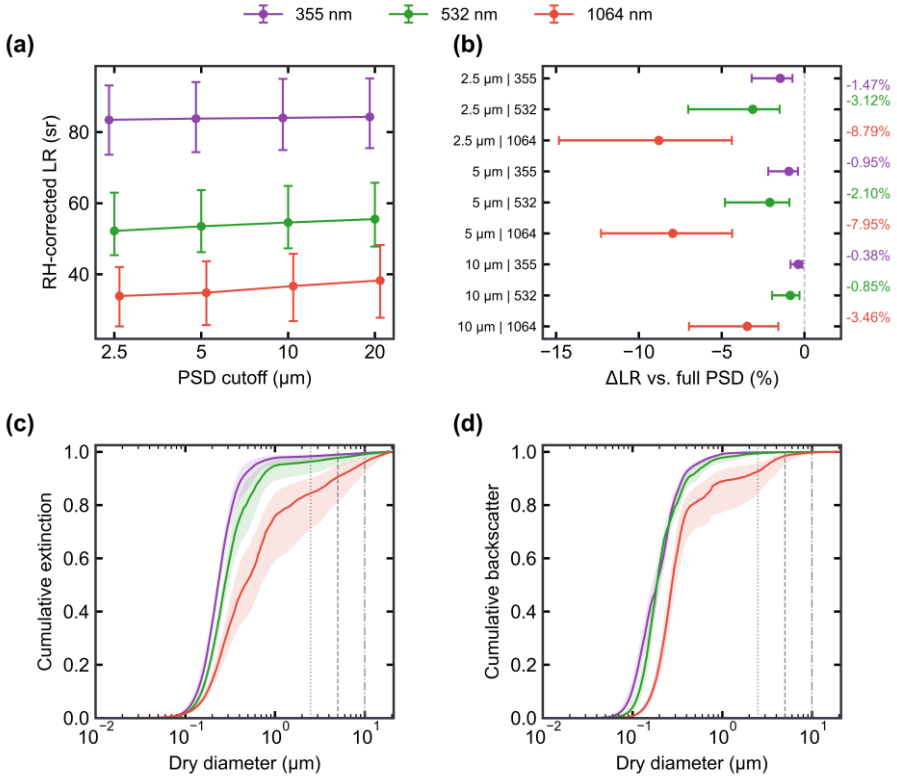


Figure S4. Sensitivity of RH-corrected optical products to upper-diameter cut-offs of 2.5, 5, and 10 µm, referenced to the full reconstructed PSD extending to approximately 20 µm (N = 304). The panels report paired LR responses and cumulative size-resolved contributions to extinction and backscatter at 355, 532, and 1064 nm. The test preserves all non-PSD assumptions and does not constitute a retrospective sampling-line correction.

These cut-off tests quantify size-support sensitivity but do not resolve particle nonsphericity. Irregular coarse particles can alter 180° backscatter and hence LR. Because hour-resolved quantitative shape constraints or collocated depolarization measurements are unavailable,

a quantitative nonsphericity correction is not applied; the retrieved CRI and optical products remain homogeneous-equivalent spherical-particle quantities.

S6 Hygroscopic-growth implementation and sensitivity to RH treatment

RH correction was applied after the dry-state inversion as a wet-state forward calculation. Collocated station RH was used as the near-surface ambient input. Additional hygroscopic growth below the operational RH reference of 40% was set to zero relative to the reference state (GF = 1), whereas values above 95% were capped at 95%. Mode-dependent κ values of 0.20 and 0.03 were prescribed for fine and coarse particles separated at D_p=1 μm (Petters and Kreidenweis, 2007; Zieger et al., 2013). Particle number was conserved, and the wet homogeneous-equivalent refractive index was calculated with Bruggeman mixing between the reference-state aerosol representation and the additional water associated with growth relative to the reference state (Bruggeman, 1935).

The growth factors were normalized to their values at RH = 40%, so that GF = 1 at the operational reference (Fig. S5a). The paired LR changes around this reference show no visible artificial step associated with the piecewise implementation (Fig. S5b). These panels are implementation diagnostics and are not used as binary robustness criteria or as validation of the prescribed κ values.

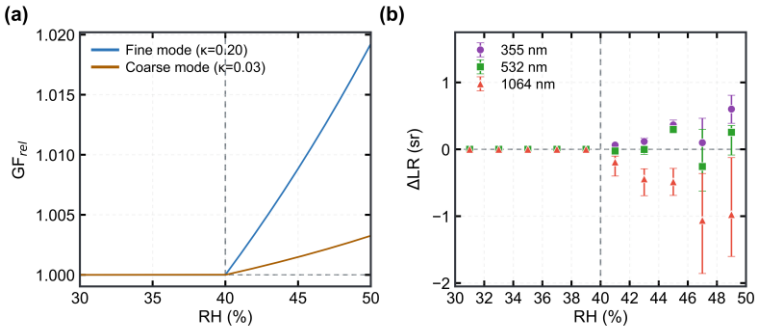


Figure S5. Implementation diagnostics for the RH-corrected forward calculation. (a) Fine- and coarse-mode growth factors referenced to RH=40%. (b) Paired changes in lidar ratio around the 40% reference, showing that the piecewise implementation does not introduce an artificial jump.

The final (N = 304) cohort contained 29 low-RH reference hours and 275 RH-active hours, including 260 hours with (40% ≤ RH ≤ 95%) and 15 hours for which RH was capped at 95%. For the RH-active subset, the median paired relative wet-minus-dry changes in extinction were +25.44%, +27.14%, and +21.04% at 355, 532, and 1064 nm, respectively, whereas the corresponding backscatter changes were +20.94%, +19.93%, and +27.44%. The corresponding median hourly paired LR changes were +1.91%, +4.15%, and −4.20%. The extinction–backscatter decomposition and its wavelength dependence are presented in Fig. 9 of the main text.

The negative median LR response at 1064 nm arose because the modeled relative backscatter enhancement exceeded the corresponding extinction enhancement (Fig. 9a in the main text). The response therefore reflects the wavelength-dependent balance between extinction and 180° backscatter after simultaneous particle growth and refractive-index dilution, rather than a monotonic increase in RH influence with wavelength. The calculation represents an ambient-equivalent near-surface sensitivity and should not be interpreted as a vertically resolved humidification correction.

S7 Aerosol-regime dependence of lidar-relevant optical products

This section summarizes the optical–microphysical context, regime definitions, and regime-resolved RH-corrected LR and SSA for the final post-QC cohort (N = 304). The FVF–AAE groupings are diagnostic optical–microphysical regimes rather than source-apportioned aerosol classes. FVF represents the fine-volume fraction of the reconstructed dry PSD, whereas $AAE_{470/880}$ summarizes the absorption spectral slope from the AE33 observations. The thresholds were applied to the final N = 304 cohort to organize retrieval behaviour without assigning unique chemical composition or emission sources. The resulting criteria and sample counts are summarized in Table S7.

Table S7. Definitions and sample counts of the FVF–AAE diagnostic regimes in the final cohort.

Regime	FVF criterion	AAE criterion	N
Coarse, lower AAE	FVF < 0.60	$AAE_{470/880} < 1.3$	38
Coarse, higher AAE	FVF < 0.60	$AAE_{470/880} \geq 1.3$	77
Intermediate FVF	$0.60 \leq FVF \leq 0.75$		103
Fine, lower AAE	FVF > 0.75	$AAE_{470/880} < 1.6$	75
Fine, higher AAE	FVF > 0.75	$AAE_{470/880} \geq 1.6$	11

S7.1 Campaign evolution of the regime diagnostics

The temporal evolution of PM_{10}, $PM_{2.5}$, eBC, AAE, RH, FVF, and effective radius provides the optical and microphysical context for the regime analysis (Fig. S6). $PM_{2.5}$ and PM_{10} were PSD-derived mass-equivalent diagnostics and were not independent mass measurements. The eBC diagnostic was calculated from AE33 absorption at 880 nm using C_{eff} = 5 and MAC_{880} = 7.77 $m^2\ g^{-1}$ and therefore was not an independent constraint on C_{eff}. For the final post-QC cohort, PM_{10}, $PM_{2.5}$, and eBC had the medians of 13.50, 10.58, and 0.25 μg m^{-3}, respectively, with corresponding maxima of 54.73, 44.85, and 2.57 μg m^{-3}, respectively. Several $PM_{2.5}$ enhancement periods coincided with elevated eBC, indicating covariation in particle loading and absorption without identifying a unique emission source.

$AAE_{470/880}$ ranged from 1.06 to 1.99, with a median of 1.43. Ambient RH had an interquartile range of 51.6–89.1%. FVF ranged from 0.259 to 0.960, while the effective radius ranged from 0.084 to 0.274 μm. These observations document transitions among coarse-influenced, intermediate, and fine-mode-dominated particle-size states and provide the basis for using FVF and AAE as diagnostic grouping variables. Gaps indicate unavailable or screened hours and were not interpolated. These time-resolved indicators define the optical–microphysical context used for the regime-resolved comparisons in Sections S7.2–S7.5.

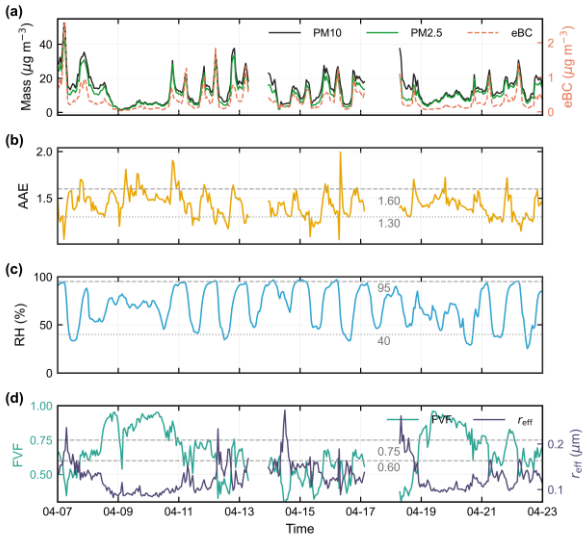


Figure S6. Temporal evolution of the optical–microphysical indicators used to define the diagnostic regimes in the final post-QC cohort. Panels show (a) PM_{10}, $PM_{2.5}$, and eBC calculated with C_{eff} = 5; (b) $AAE_{470/880}$; (c) relative humidity; and (d) FVF and effective radius. Horizontal reference lines identify the RH and FVF thresholds used in the diagnostic analysis. Displayed gaps correspond to unavailable or screened hours and are not interpolated.

S7.2 Regime-resolved RH-corrected lidar ratio and SSA

Figure S7 shows that RH-corrected LR and SSA vary systematically across the five FVF–AAE regimes.

RH-corrected SSA generally increases from coarse-influenced to fine-mode-dominated conditions, with a stronger coarse–fine contrast at 355 and 532 nm than at 1064 nm. The AAE subdivision further modulates the distributions; in particular, the fine-mode higher-AAE group retains a steeper wavelength dependence of absorption.

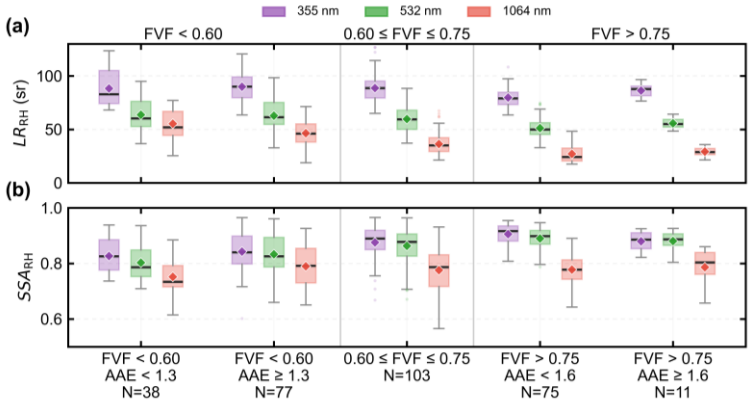


Figure S7. Distributions of RH-corrected lidar ratio and SSA across the FVF–AAE diagnostic regimes in the final *N* = 304 cohort. Panels show (a) LR and (b) SSA at 355, 532, and 1064 nm. Regimes are defined using FVF and $AAE_{470/880}$ as listed in Table S7.

S7.3 FVF-dependent lidar-ratio spectra

Figure S8 summarizes the FVF-dependent spectral profiles of RH-corrected LR. All broad FVF groups show decreasing LR from 355 to 1064 nm, but the magnitude of the decrease depends strongly on particle-size regime. In the current post-QC cohort, the coarse-influenced group (FVF<0.60, N=115) has median LR values of 89.87, 61.25, and 48.90 sr at 355, 532, and 1064 nm, respectively. The fine-dominated group (FVF>0.75, N=86) has corresponding medians of 78.31, 48.28, and 25.05 sr. Thus, the fine-dominated group exhibits a substantially stronger decrease toward 1064 nm. AAE is shown only to provide absorption-spectral context and is not treated as an independent effect estimate.

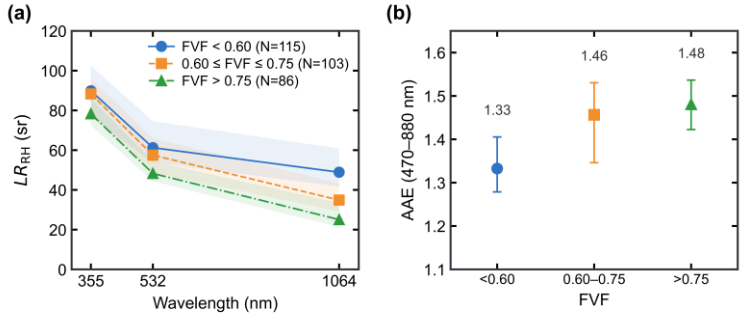


Figure S8. FVF-dependent RH-corrected lidar-ratio spectra at 355, 532, and 1064 nm for the final *N* = 304 cohort. The broad FVF categories represent coarse-influenced, intermediate, and fine-dominated particle-size states.

S7.4 Regime dependence of the AE33 correction sensitivity

Figure S9 shows that increasing C_{eff} generally increases SSA_{355} and decreases LR_{355} in all FVF–AAE regimes because the corrected AE33 absorption input decreases as C_{eff} increases. The response is strongest between C_{eff} = 1.57 and 3.0 and becomes weaker at larger C_{eff}. The persistence of regime separation across the tested range shows that the absorption-correction assumption changes the retrieved magnitude while its effect is modulated by both particle-size structure and absorption spectral dependence. The fine-mode lower-AAE regime retains comparatively high SSA and low LR_{355}, whereas the fine-mode higher-AAE regime maintains higher LR_{355}, consistent with its steeper wavelength dependence of absorption. These calculations are sensitivity tests; they do not calibrate a campaign-specific C_{eff}.

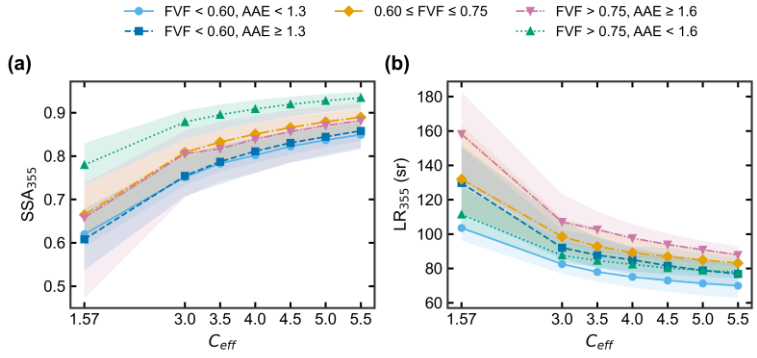


Figure S9. Regime-dependent sensitivity of RH-corrected SSA355 and LR_{355} to the AE33 effective multiple-scattering correction factor C_{eff} in the final N = 304 cohort. Lines indicate regime medians, and shaded envelopes show interquartile ranges. C_{eff} is varied as a structural sensitivity parameter rather than an independently calibrated campaign constant.

S7.5 Fine- and coarse-mode contribution and interpretation limits

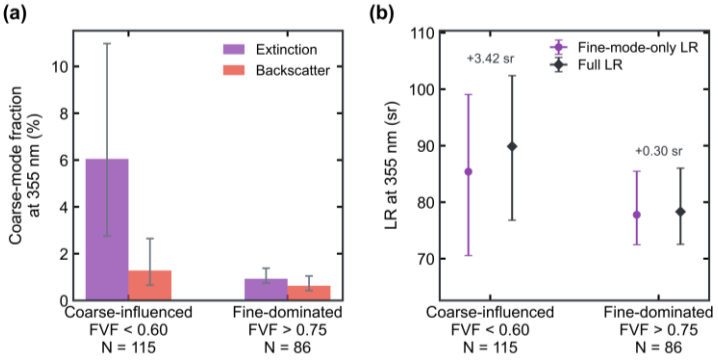


Figure S10. Fine/coarse mode decomposition of the 355 nm RH-corrected lidar ratio difference between FVF regimes. (a) Relative coarse-mode contributions to extinction and backscatter. (b) Comparison between fine-mode-only and full LR_{355}, showing the contribution of coarse-mode inclusion. Error bars denote interquartile ranges; annotations show the medians of the hourly paired full-minus-fine-mode-only differences.

To examine the higher LR_{355} in the coarse-influenced subset, the coarse-influenced FVF < 0.60, N=115 and fine-dominated FVF > 0.75, N=86 subsets were decomposed at 355 nm using a dry-particle diameter of D_p=1 μm as the mode boundary (Fig. S10). The coarse mode accounted for median fractions of 6.05 % of total extinction and 1.28 % of total backscatter in the coarse-influenced subset, compared with 0.93 % and 0.63 % in the fine-dominated subset. Its inclusion increased LR_{355} relative to the fine-mode-only calculation by median paired values of 3.42 and 0.30 sr, respectively. However, the fine-mode-only medians also differed between the subsets (85.40 versus 77.77 sr). The coarse mode therefore enhanced, but did not fully account for, the between-subset contrast. This diagnostic decomposition does not imply a unique aerosol type, composition, or source.

References

Bruggeman, D. A. G.: Berechnung verschiedener physikalischer Konstanten von heterogenen Substanzen. I. Dielektrizitätskonstanten und Leitfähigkeiten der Mischkörper aus isotropen Substanzen, Ann. Phys., 416, 636–664, https://doi.org/10.1002/andp.19354160705, 1935.

Di Antonio, L., Di Biagio, C., Formenti, P., Gratien, A., Michoud, V., Cantrell, C., Bauville, A., Bergé, A., Cazaunau, M., Chevaillier, S., Cirtog, M., Coll, P., D'Anna, B., de Brito, J. F., De Haan, D. O., Dignum, J. R., Deshmukh, S., Favez, O., Flaud, P.-M., Gaimoz, C., Hawkins, L. N., Kammer, J., Language, B., Maisonneuve, F., Močnik, G., Perraudin, E., Petit, J.-E., Acharja, P., Poulain, L., Pouyes, P., Pronovost, E. D., Riffault, V., Roundtree, K. I., Shahin, M., Siour, G., Villenave, E., Zapf, P., Foret, G., Doussin, J.-F., and Beekmann, M.: Aerosol spectral optical properties in the Paris urban area and its peri-urban and forested surroundings during summer 2022 from ACROSS surface observations, Atmos. Chem. Phys., 25, 3161–3189, https://doi.org/10.5194/acp-25-3161-2025, 2025.

Lill, E., Costa, E. J., Barry, K., Mirrielees, J. A., Mashkevich, M., Wu, J., Holen, A. L., Cesler-Maloney, M., DeMott, P. J., Perkins, R., Hill, T., Sullivan, A., Levin, E., Simpson, W. R., Mao, J., Temime-Roussel, B., D'Anna, B., Law, K. S., Ault, A. P., Schmitt, C., Pratt, K. A.,

Fischer, E. V., and Creamean, J.: The abundance and sources of ice nucleating particles within Alaskan ice fog, J. Geophys. Res.-Atmos., 129, e2024JD041170, https://doi.org/10.1029/2024JD041170, 2024.

Petters, M. D. and Kreidenweis, S. M.: A single parameter representation of hygroscopic growth and cloud condensation nucleus activity, Atmos. Chem. Phys., 7, 1961–1971, https://doi.org/10.5194/acp-7-1961-2007, 2007.

Sinyuk, A., Holben, B. N., Eck, T. F., Giles, D. M., Slutsker, I., Korkin, S., Schafer, J. S., Smirnov, A., Sorokin, M., and Lyapustin, A.: The AERONET Version 3 aerosol retrieval algorithm, associated uncertainties and comparisons to Version 2, Atmos. Meas. Tech., 13, 3375–3411, https://doi.org/10.5194/amt-13-3375-2020, 2020.

Yus-Díez, J., Drinovec, L., Alados-Arboledas, L., Titos, G., Bazo, E., Casans, A., Patrón, D., Querol, X., Gonzalez-Romero, A., Perez García-Pando, C., and Močnik, G.: Characterization of filter photometer artifacts in soot and dust measurements – laboratory and ambient experiments using a traceably calibrated aerosol absorption reference, Atmos. Meas. Tech., 18, 3073–3093, https://doi.org/10.5194/amt-18-3073-2025, 2025.

Zieger, P., Fierz-Schmidhauser, R., Weingartner, E., and Baltensperger, U.: Effects of relative humidity on aerosol light scattering: results from different European sites, Atmos. Chem. Phys., 13, 10609–10631, https://doi.org/10.5194/acp-13-10609-2013, 2013.

Zinke, J., Nilsson, E. D., Markuszewski, P., Zieger, P., Mårtensson, E. M., Rutgersson, A., Nilsson, E., and Salter, M. E.: Sea spray emissions from the Baltic Sea: comparison of aerosol eddy covariance fluxes and chamber-simulated sea spray emissions, Atmos. Chem. Phys., 24, 1895–1918, https://doi.org/10.5194/acp-24-1895-2024, 2024.